iScience

CellPress
OPEN ACCESS

Article

Lipid bilayer-assisted dynamic self-assembly of hexagonal DNA origami blocks into monolayer crystalline structures with designed geometries

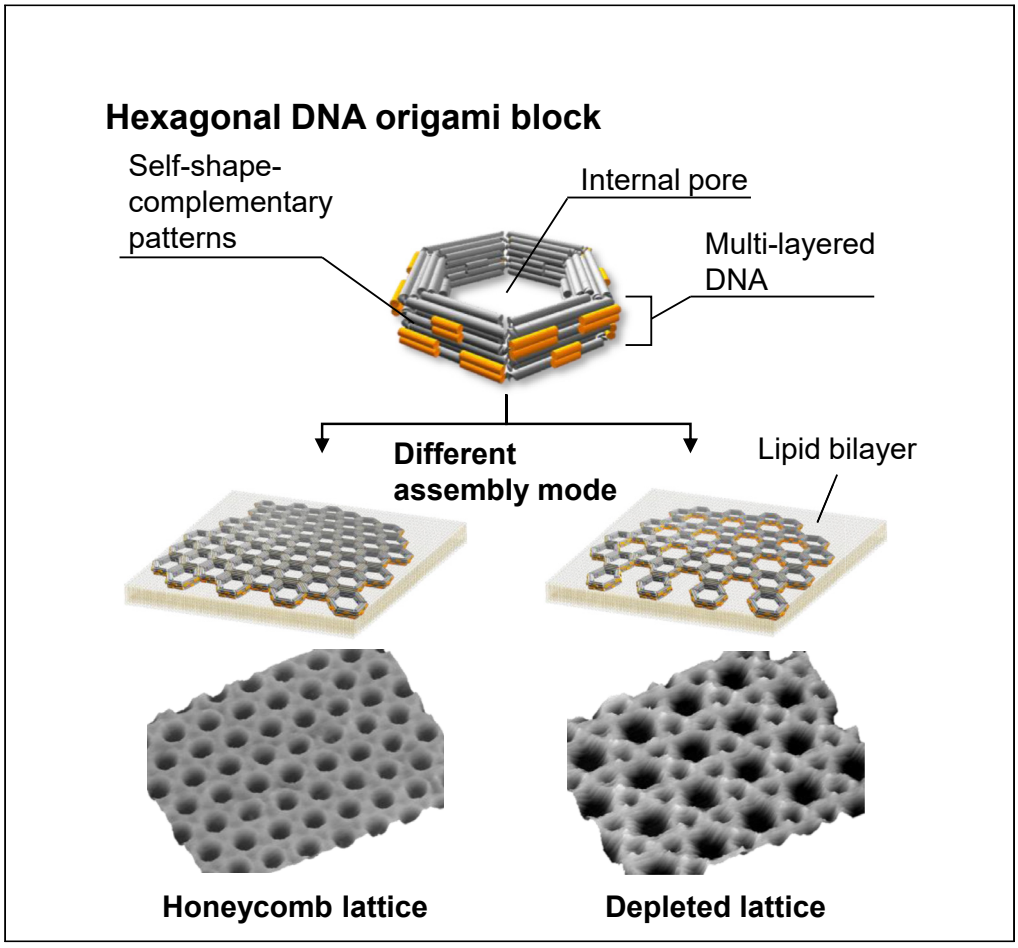

Yuki Suzuki, Ibuki Kawamata, Kotaro Watanabe, Eriko Mano

yuki.suzuki.e6@tohoku.ac.jp

Highlights

Lipid bilayer-assisted self-assembly of 3D DNA origami blocks was achieved

Time-lapse AFM imaging of the self-assembly processes was performed

Different assembly patterns were achieved from a single DNA origami design

Suzuki et al., iScience *25*, 104292
May 20, 2022 © 2022 The Authors.
https://doi.org/10.1016/j.isci.2022.104292

iScience

CellPress
OPEN ACCESS

Article

Lipid bilayer-assisted dynamic self-assembly of hexagonal DNA origami blocks into monolayer crystalline structures with designed geometries

Yuki Suzuki,[1,3,4,*] Ibuki Kawamata,[2] Kotaro Watanabe,[2] and Eriko Mano[1]

SUMMARY

The DNA origami technique is used to construct custom-shaped nanostructures that can be used as components of two-dimensional crystalline structures with user-defined structural patterns. Here, we designed an Mg^{2+}-responsive hexagonal 3D DNA origami block with self-shape-complementary ruggedness on the sides. Hexagonal DNA origami blocks were electrostatically adsorbed onto a fluidic lipid bilayer membrane surface to ensure lateral diffusion. A subsequent increase in the Mg^{2+} concentration in the surrounding environment induced the self-assembly of the origami blocks into lattices with prescribed geometries based on a self-complementary shape fit. High-speed atomic force microscopy (HS-AFM) images revealed dynamic events involved in the self-assembly process, including edge reorganization, defect splitting, diffusion, and filling, which provide a glimpse into how the lattice structures are self-improved.

INTRODUCTION

Molecular self-assembly has attracted considerable attention as a method for the construction of novel supramolecular architectures. The scaffolded DNA origami method has enabled the one-pot preparation of almost arbitrarily shaped two-dimensional (2D) (Rothemund, 2006) and three-dimensional (3D) DNA nanostructures (Andersen et al., 2009; Dietz et al., 2009; Douglas et al., 2009a; Han et al., 2011; Kuzuya and Komiyama, 2009), which can be further used as components of higher-order architectures that self-assemble based on intermolecular interactions between DNA ends, such as sticky-ended cohesion (Liu et al., 2011; Rajendran et al., 2011; Tikhomirov et al., 2017; Zhang et al., 2018; Zhao et al., 2011) and blunt-ended stacking (Wagenbauer et al., 2017; Woo and Rothemund, 2011).

Among the various assembly approaches, mica-surface-assisted self-assembly (mica-SAS) is a promising method to obtain two-dimensionally ordered arrays of 2D DNA origamis (Aghebat Rafat et al., 2014; Kielar et al., 2018; Ramakrishnan et al., 2016; Woo and Rothemund, 2014; Xin et al., 2021). One key to the success of mica-SAS is the setting of appropriate adsorption conditions (i.e., not too weak and not too strong) to ensure the surface mobility of the component DNA origami on the mica substrate. In general, DNA origami structures are prepared in a buffer solution containing 10–20 mM Mg^{2+} in which they are strongly adsorbed onto mica surfaces and do not exhibit two-dimensional diffusion. Therefore, for the mica-SAS of DNA origami crystals, 200–700 mM NaCl was added to weaken the electrostatic interaction between DNA and the mica surface (Aghebat Rafat et al., 2014; Woo and Rothemund, 2014).

This strategy has been well established for the construction of monolayered crystalline structures from 2D DNA origami, but cannot be simply applied to those from 3D DNA origami, especially those that require high Mg^{2+} concentrations to connect with each other. Representative examples of such structures include the 3D DNA origami blocks with shape-complementary recession-protrusion patterns proposed by Gerling et al. (2015). These structures can be multimerized based on shape-fitting upon increasing the Mg^{2+} concentration, to neutralize the electrostatic repulsion between the shape-complementary interfaces. However, this type of assembly mechanism is unsuitable for conventional mica-SAS as increasing Mg^{2+} also strengthens the adsorption of DNA origami blocks onto the mica surface, making them immobile. Increasing the Na^{+} concentration is also unfeasible in this case due to its inhibitory effect on the multivalent cation-induced DNA-DNA interactions (Hibino et al., 2006).

[1]Frontier Research Institute for Interdisciplinary Sciences, Tohoku University, 6-3 Aramaki-aza Aoba, Aoba-ku, Sendai 980-8578, Japan

[2]Department of Robotics, Graduate School of Engineering, Tohoku University, 6-6-01 Aramaki-aza Aoba, Aoba-ku, Sendai 980-8579, Japan

[3]Present address: Division of Chemistry for Materials, Graduate School of Engineering, Mie University, 1577 Kurimamachiya-cho, Tsu, Mie 514–8507, Japan

[4]Lead contact

*Correspondence: yuki.suzuki.e6@tohoku.ac.jp

https://doi.org/10.1016/j.isci.2022.104292

This is an open access article under the CC BY-NC-ND license (http://creativecommons.org/licenses/by-nc-nd/4.0/).

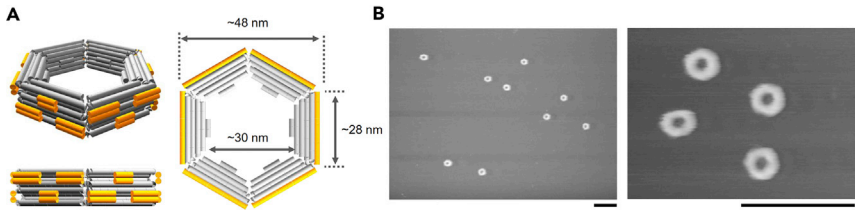

Figure 1. Three-dimensional hexagonal DNA origami blocks (3D-Hx) with self-complementary ruggedness (protrusion-recession patterns) on the sides

(A) Schematic illustration of 3D-Hx. Adjacent sides of 3D-Hx showing upside-down patterns of the ruggedness. See also Video S1 for the structural design.

(B) Atomic force microscopy (AFM) image of the purified 3D-Hx. Scale bars: 200 nm.

To reconcile these conflicts, we employed the lipid bilayer-surface-assisted self-assembly (LB-SAS) (Avakyan et al., 2017; Kempter et al., 2019; Kocabey et al., 2015; Suzuki et al., 2015) to assemble Mg^{2+}-responsive 3D DNA origami blocks into monolayered crystalline structures. Artificial lipid bilayers, especially glass- or mica-supported lipid bilayers (SLBs), provide a flat but dynamic surface with the desired physicochemical properties (such as fluidity and surface charge) by tuning their lipid compositions, which enables us to realize conditions to ensure the lateral mobility of assembly components. In this study, we designed a 3D DNA origami block whose sides exhibited self-shape-complementary ruggedness. The electrostatic adsorption of DNA origami blocks onto a fluidic lipid bilayer membrane allows their diffusion on the surface. The subsequent increase in Mg^{2+} promotes their self-assembly into a lattice with a designed geometry through homomultimerization based on a self-complementary shape-fit. The utilization of block-shaped components with prescribed thickness expands the constructible structures, whose thickness has been limited to ~2 nm in the conventional assemblies of sheet-like 2D DNA origami structures, *via* a surface-assisted approach. Our study provides a general approach for the construction of custom DNA origami lattices with the desired assembly patterns and nanoporous structures that will serve not only as a nano-micro scaffold for molecular patterning but also as an array of nanocompartmentalized spaces.

RESULTS AND DISCUSSIONS

Design of a hexagonal DNA origami block

As the self-assembly component, we designed a hexagonal 3D DNA origami using caDNAno2 (Figure 1A, see also Figure S1) (Douglas et al., 2009b). The sides of the hexagonal 3D origami (3D-Hx) exhibited shape-complementary ruggedness (Video S1), which imposes self-complementary shape-fitting to allow assembly into a homomultimeric two-dimensional lattice (Gerling et al., 2015). The 3D-Hx was prepared by annealing a mixture of 8064 nt scaffold DNA (p8064) and staple strands in folding buffer (5 mM Tris-HCl [pH 8.0], 15 mM $MgCl_2$, and 5 mM EDTA), and then purified using a glycerol gradient (Lin et al., 2013) (STAR Methods, Figure S2). Atomic force microscopy (AFM) imaging (Figure 1B) revealed the monodispersed nature of the purified 3D DNA origami blocks, with a size of 53 $\pm$ 4 nm (mean $\pm$ S.D., N = 85), which is in good agreement with the expected size.

2D self-assembly on the mica-supported lipid bilayer membrane

The purified 3D-Hx was self-assembled into honeycomb lattices on a mica-supported 1,2-dioleoyl-*sn*-glycero-3-phosphocholine (DOPC) bilayer. In this experiment, 3D-Hx was first adsorbed onto the DOPC bilayer in folding buffer (5 mM Tris-HCl [pH 8.0], 15 mM $MgCl_2$, and 1 mM EDTA). The concentration of Mg^{2+} was then increased to reduce electrostatic repulsions among the negatively charged DNA origami interfaces, leading to shape-complementary fittings among the ruggedness of the 3D-Hxs, which were further stabilized *via* blunt-ended interactions (Figure 2A). Although several defects remained in the assembled lattices, high-magnification AFM images revealed the periodic features of the honeycomb lattice, comprising internal cavities with a depth of 11 $\pm$ 1 nm and a distance between opposite sides of 27 $\pm$ 2 nm (N = 133) (Figures 2B and 2C, see also Figure S3).

Dynamic events involved in lattice formation

Dynamic events, such as boundary reorganization, defect diffusion, and defect filling, occurring on an SLB were successfully monitored using time-lapse AFM imaging. Figure 3A shows the representative

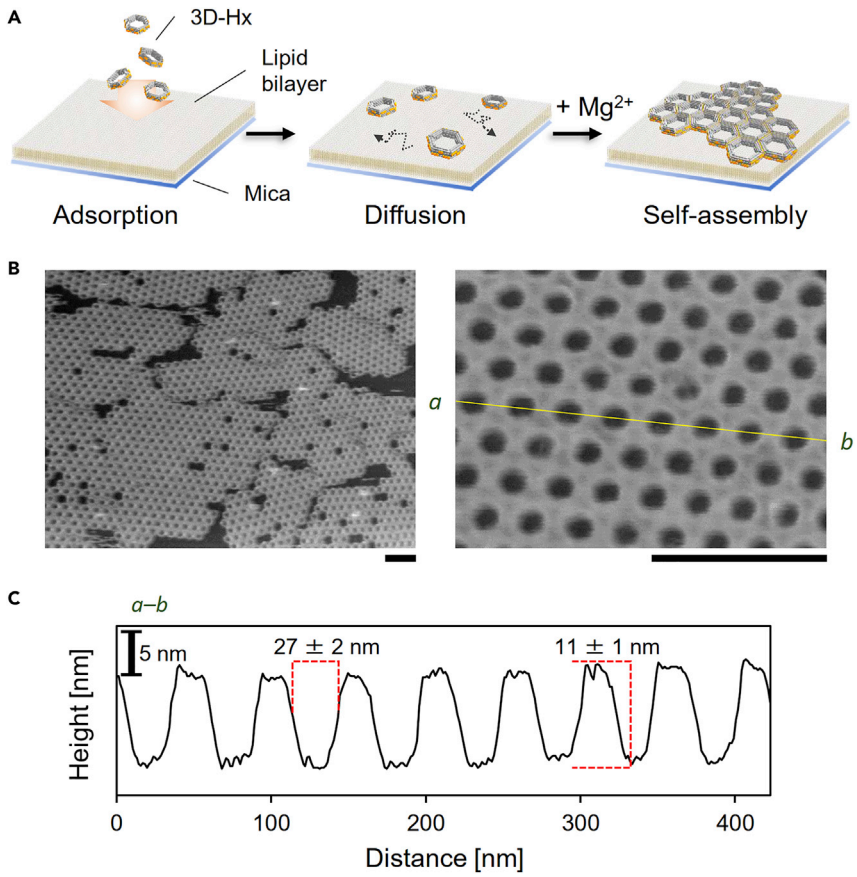

Figure 2. Lipid bilayer-assisted self-assembly of 3D-Hx into a honeycomb lattice

(A) Schematic of the experimental procedure. 3D-Hx is deposited onto the mica-supported lipid bilayer membrane (mica-SLB). The connection among 3D-Hx blocks are then induced by increasing Mg^{2+} concentration of the surrounding environment (buffer solution).

(B) AFM image of the honeycomb lattice assembled on the mica-SLB. Scale bars: 200 nm.

(C) Cross-sectional profile along the line *a*-*b* in (B). Errors represent standard deviations.

sequential images obtained after increasing the [Mg^{2+}] to 50 mM (Video S2). The dynamic association and dissociation of 3D-Hx monomers and oligomers frequently occur around the edges of the lattices (See also another example in Video S3). It should be noted that the area occupied by 3D-Hxs in the image area gradually increased with fluctuations in its value (Figure S4), indicating that diffusing 3D-Hxs entered and exited the area, some of which were incorporated into the already existing lattices. In particular, the main lattice island in the scanning area (Figures 3A, 0 s) increased with the incorporation of 3D-Hxs. Intriguingly, 3D-Hx monomers and oligomers dissociated from adjacent lattices were also incorporated into this lattice.

Dissociation and re-association of the components occur not only at the edges of the lattices but also at the defects in the assembled lattice, resulting in defect diffusion. In the example shown in Figure 3B (see also Video S4), a defect equivalent of triangularly arranged 3 hexagonal blocks was observed in the initial frame. This defect split into a single defect and a twin defect, the latter of which moved from the left to the right of the image area, while the single defect remained at the same position. Figure 3C depicts another dynamic event, in which a large defect was reduced by incorporating 3D-Hx monomers. In the initial frame of this example (Figure 3C, see also Video S5), a large defect equivalent to seven hexagonal blocks was observed. The first monomer, which remained unadsorbed on the SLB surface, jumped into this defect, attempting to make a connection with the upper edge of the defect, but soon moved to the lower edge to make a tentative connection, indicating that the connection at the two sides was not sufficiently strong for the incorporation of the monomer into the already assembled lattice at this Mg^{2+} concentration (50 mM). After the

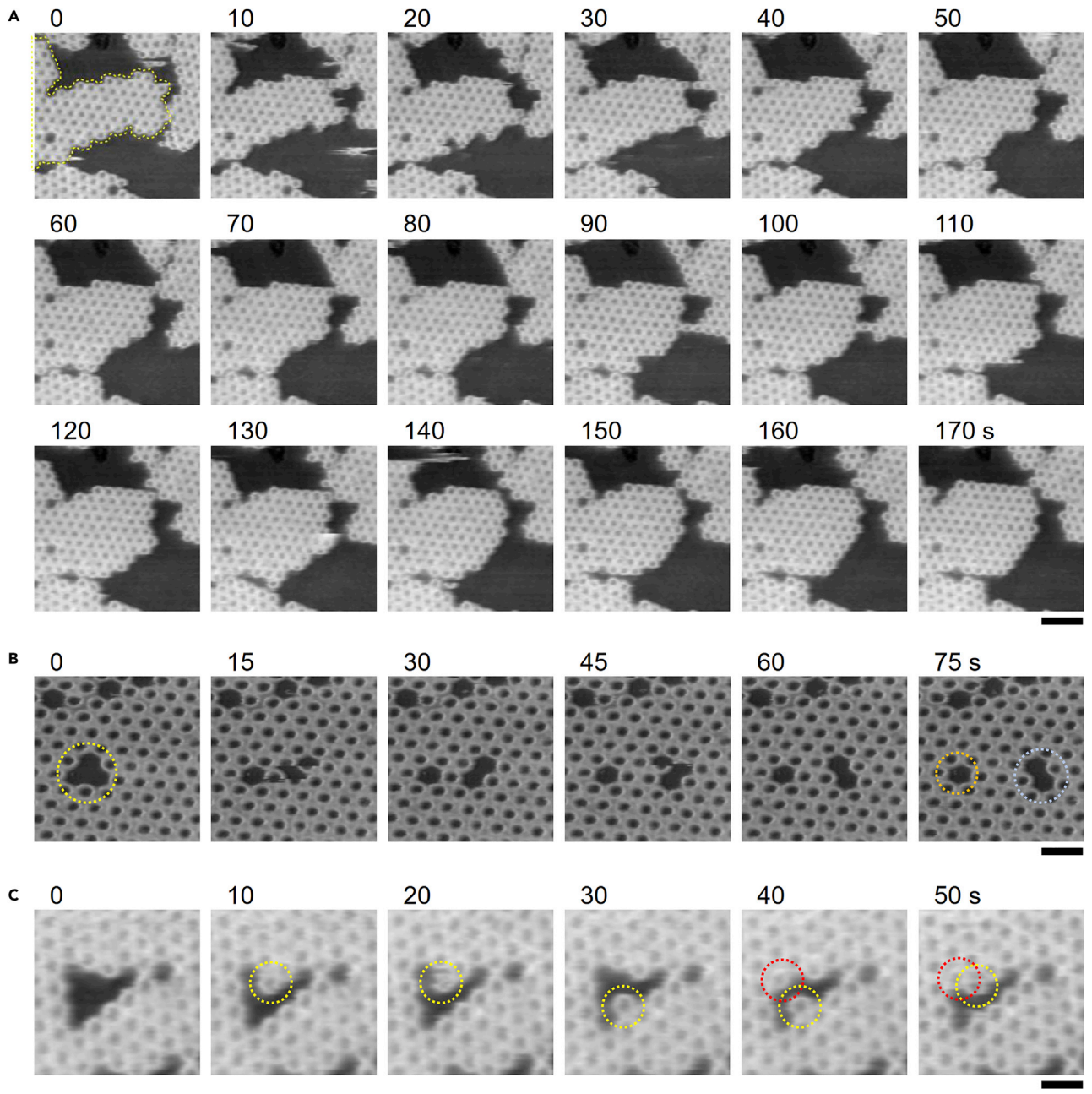

Figure 3. Dynamic events involved in lattice formation

(A) Lattice growth monitored using high-speed AFM (HS-AFM). Region surrounded by dashed yellow line in the initial frame exhibited dynamic growth. Scale bar: 200 nm. Images were recorded at a scan rate of 0.5 frames per second (fps). For the complete movie, see Video S2.

(B) Defect splitting and defect diffusion monitored using HS-AFM. The defect indicated by yellow circle (0 s) split into a single defect (orange dashed circle, 75 s) and a twin defect (light blue dashed circle, 75 s). Scale bar: 100 nm. Images were recorded at a scan rate of 0.2 fps. For the complete movie, see Video S4.

(C) Defect filling was monitored using HS-AFM. The first and second monomers jumped into the defect and are indicated by dashed yellow and red circles, respectively. Scale bar: 100 nm. Images were recorded at a scan rate of 0.5 fps. For the complete movie, see Video S5.

arrival of the second monomer, the first monomer again moved to the upper side and was incorporated into the lattice with the second monomer. Both the first and second monomers made connections on three of the six sides in the last frame. These observations provide a glimpse into how defects arising in the assembly process become smaller.

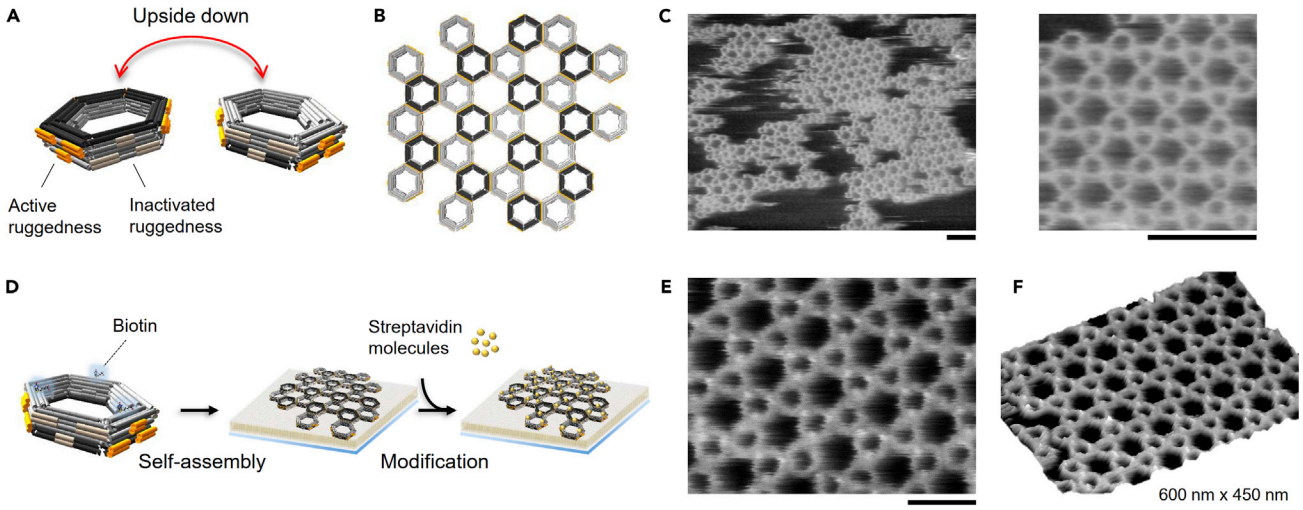

Figure 4. Lipid bilayer-assisted self-assembly of 3D-Hx into a depleted honeycomb lattice

(A) Schematic of the variation of the 3D-Hx whose ruggedness at three symmetric sides are inactivated. Active ruggedness and inactivated ruggedness are colored with orange and light orange, respectively. For convenience, the obverse and reverse of the 3D-Hx are indicated by different colors.

(B) Schematic illustration of the depleted honeycomb lattice.

(C) AFM image of the depleted honeycomb lattice assembled on the mica-SLB. Scale bars: 200 nm.

(D) Schematic of the experimental procedure of the post-assembly modification with streptavidin molecules.

(E) AFM images of the streptavidin-bound depleted honeycomb lattice. Scale bar: 100 nm.

(F) Surface plot of the streptavidin-bound depleted honeycomb lattice.

Self-assembly into depleted lattice and its surface modification

One of the unique features of this system is that we can inactivate the designated sides by disabling blunt-ended interactions through the addition of polyT tails at the ends of the protruding parts of the ruggedness. This simple customizability enabled us to realize different assembly modes of 3D-Hx. Here, ruggedness at the three symmetrical sides of the 3D-Hx was inactivated by staple extension with polyT tails (Figure 4A S5). Because the adjacent sides of our 3D-Hx origami showed upside-down patterns of ruggedness (Video S1, Figure S1), self-assembly of this 3-symmetric-side-inactivated hexagonal block (3D-Hx-135) resulted in a "depleted" honeycomb lattice in which face-down and face-up blocks are alternately laid out (Figure 4B). AFM images of the assembled lattices revealed structural features in which pores of two different sizes were arranged (Figure 4C and S6). To address the facing orientation of the 3D-Hx-135 blocks in the depleted honeycomb lattice, we prepared a functionalized block, with one of the faces having three biotin moieties, and performed post-self-assembly modification (Figure 4D). The depleted lattice was first prepared on the bilayer from one-sided biotinylated blocks. After lattice formation was confirmed, streptavidin was loaded onto the same sample. With this post-assembly treatment, only the blocks facing upwards could bind streptavidin. Figure 4E and 4F shows a representative AFM image after the post-assembly modification, where every other block in the lattice was decorated, demonstrating facing-up (modified) blocks and facing-down (unmodified) blocks alternately arranged in the depleted lattice, as expected.

Conclusion

Herein, we designed an Mg^{2+}-responsive hexagonal 3D DNA origami block with self-complementary features and demonstrated its ability to form LB-SAS in lattices with prescribed structural patterns. The primary advantage of the self-shape-complementary design employed here is that it can inactivate connections at arbitrary sides by simply extending the polyT tails from blunt ends. This enables the construction of lattices with different patterns from a single 3D DNA origami block design. To satisfy the conditions that allow both the surface diffusion of the origami blocks and their Mg^{2+}-induced assembly, we employed an artificial lipid bilayer membrane as a soft and flat surface to serve as an alternative to the naked mica surface. The lipid bilayer-adsorbed origami blocks retained their surface mobility and self-assembled into lattices with the desired geometries, in a process involving edge reorganization, defect splitting, diffusion, and filling, in response to the changes in Mg^{2+} concentration in the surrounding environment.

In our protocol for DNA origami preparation, four times the excess amount of staple strands are mixed against a scaffold DNA (p8064, 0.75 USD per pmol). Because each staple DNA costs 0.12 USD per base at a molar yield of 10 nmol and 7596 bases of the scaffold were folded into a designed shape with staples, total cost of the origami per pmol is 1.1 USD (i.e., 1.8×10^{-12} USD per origami). Given that the area occupied by a single hexagonal DNA block is about 1.5×10^{-11} cm^2 (1500 nm^2), the cost of the DNA required to assemble the honeycomb lattice is estimated to be 0.12 USD per cm^2, which is comparable to the cost required for the mica-assisted self-assembly of conventional 2D DNA origami lattices (Xin et al., 2021). This cost can be lowered, owing to the development of methods for the mass production of DNA strands (Praetorius et al., 2017) and the further improvement of DNA synthesis technology.

Lipid membrane-interacting DNA nanostructures have recently attracted great attention in the fields of synthetic biology (Czogalla et al., 2016) and molecular robotics (Hagiya et al., 2014) for their potential to mimic the structures and functions of membrane proteins (Burns et al., 2013, 2016; Krishnan et al., 2016; Langecker et al., 2012; Thomsen et al., 2019), membrane-binding proteins (Czogalla et al., 2015; Franquelim et al., 2018; Grome et al., 2018; Khmelinskaia et al., 2018), and membrane-cytoskeleton networks (Kocabey et al., 2015; Kurokawa et al., 2017). We believe that our approach to assembling lattices with 3D features matches with this direction, not just for its application as a scaffold for the periodic placement of protein molecules and metal nanoparticles.

Other possible applications may result from the use of nanospaces compartmentalized by origami blocks. It has been implicated that reaction kinetics of various biological molecules in the nanoconfinement spaces differ from those in bulk solutions (Kuchler et al., 2016). DNA origami nanotechnology has enabled the construction of a designed 3D nanospace, in which a single to several molecules of interest are enclosed and applied to reveal the effects of nanoconfinement on enzymatic reactions (Grossi et al., 2017; Zhao et al., 2016) and the structural transitions of DNA (Jonchhe et al., 2018; Shrestha et al., 2017). The porous crystalline DNA origami structures can be regarded as arrays of such nanoconfinement spaces, which provide a tool for multiplexed single-molecule analysis (Sakamoto et al., 2020) that will enable the simultaneous monitoring of reactions occurring in individual nanopores.

Limitations of the study

One of the primary limitations of this study is that in our origami design and surface-assisted approach, self-assembly fundamentally occurs in 2D, although the assembly component itself is a 3D object. However, extending the assembling process into 2nd, 3rd, or more layers could be investigated in the future by designing interactions between the top and bottom faces of the origami block. Introducing specific interactions among multiple different components, which should lead to the surface-assisted self-assembly of lattices with predetermined shapes and sizes, will also be challenging.

Our 3D-Hx can be regarded as a modular structure because we can prevent an arbitral side from connecting with others by disabling blunt-end stacking *via* staple extension with polyT. However, the current design has a symmetric appearance and thus does not allow us to define the combination of sides to be connected, as only one type of shape-complementary ruggedness is employed. This drawback should be addressed by designing specific pairs of complementary ruggedness patterns at specific pairs of sides. Such strategy could be applied not only to our hexagonal blocks but also to other 3D structures, such as cubes and cuboids. The implementation of photoresponsive moieties (Asanuma et al., 2007; Kamiya and Asanuma, 2014; Yoshimura and Fujimoto, 2008) to control the blunt-ended stacking (Gerling and Dietz, 2019; Willner et al., 2017) is also a fascinating direction, which would enable *in situ* switching of the assembly mode of the DNA origami component, thus leading to controlled reorganization of the lattice geometry from honeycomb to depleted, and *vice versa*.

STAR★METHODS

Detailed methods are provided in the online version of this paper and include the following:

- KEY RESOURCES TABLE
- RESOURCE AVAILABILITY
  - Lead contact
  - Materials availability
  - Data and code availability

CellPress
OPEN ACCESS

SUPPLEMENTAL INFORMATION

Supplemental information can be found online at https://doi.org/10.1016/j.isci.2022.104292.

ACKNOWLEDGMENTS

The authors would like to thank S. M. Nomura and S. Murata (Tohoku University) for their help with the ultracentrifugation. Y.S. would like to thank N. Sakai for providing the technical assistance. This work was supported by the Japan Society for the Promotion of Science (JSPS) Grant-in-Aid for Scientific Research (KAKENHI; grant numbers 18K19831, 18KK0139, 19H04201, and 21H05864 to Y.S. and 18K18144 to I.K.). Support from the 51st Research Grants in the Natural Sciences of Mitsubishi Foundation to I. K. and support from the Building of Consortia for the Development of Human Resources in Science and Technology to Y. S. are also acknowledged.

AUTHOR CONTRIBUTIONS

The manuscript was written largely by Y.S., with sections contributed by I.K. Y.S. and I.K. designed the hexagonal DNA origami block. Y.S. performed AFM experiments. Y.S., E.M., and K.W. performed biochemical experiments and analysis. All the authors approved the final manuscript.

DECLARATION OF INTERESTS

The authors declare no competing interests.

Received: January 5, 2022
Revised: March 18, 2022
Accepted: April 19, 2022
Published: May 20, 2022

REFERENCES

Aghebat Rafat, A., Pirzer, T., Scheible, M.B., Kostina, A., and Simmel, F.C. (2014). Surface-assisted large-scale ordering of DNA origami tiles. Angew. Chem. Int. Ed. *53*, 7665–7668. https://doi.org/10.1002/anie.201403965.

Andersen, E.S., Dong, M., Nielsen, M.M., Jahn, K., Subramani, R., Mamdouh, W., Golas, M.M., Sander, B., Stark, H., Oliveira, C.L.P., et al. (2009). Self-assembly of a nanoscale DNA box with a controllable lid. Nature *459*, 73–76. https://doi.org/10.1038/nature07971.

Asanuma, H., Liang, X., Nishioka, H., Matsunaga, D., Liu, M., and Komiyama, M. (2007). Synthesis of azobenzene-tethered DNA for reversible photoregulation of DNA functions: hybridization and transcription. Nat. Protoc. *2*, 203–212. https://doi.org/10.1038/nprot.2006.465.

Avakyan, N., Conway, J.W., and Sleiman, H.F. (2017). Long-range ordering of blunt-ended DNA tiles on supported lipid bilayers. J. Am. Chem. Soc. *139*, 12027–12034. https://doi.org/10.1021/jacs.7b06572.

Burns, J.R., Gopfrich, K., Wood, J.W., Thacker, V.V., Stulz, E., Keyser, U.F., and Howorka, S. (2013). Lipid-bilayer-spanning DNA nanopores with a bifunctional porphyrin anchor. Angew. Chem. Int. Ed. *52*, 12069–12072. https://doi.org/10.1002/anie.201305765.

Burns, J.R., Seifert, A., Fertig, N., and Howorka, S. (2016). A biomimetic DNA-based channel for the ligand-controlled transport of charged molecular cargo across a biological membrane. Nat. Nanotechnol. *11*, 152–156. https://doi.org/10.1038/nnano.2015.279.

Czogalla, A., Franquelim, H.G., and Schwille, P. (2016). DNA nanostructures on membranes as tools for synthetic biology. Biophy. J. *110*, 1698–1707. https://doi.org/10.1016/j.bpj.2016.03.015.

Czogalla, A., Kauert, D.J., Franquelim, H.G., Uzunova, V., Zhang, Y., Seidel, R., and Schwille, P. (2015). Amphipathic DNA origami nanoparticles to scaffold and deform lipid membrane vesicles. Angew. Chem. Int. Ed. *54*, 6501–6505. https://doi.org/10.1002/anie.201501173.

Dietz, H., Douglas, S.M., and Shih, W.M. (2009). Folding DNA into twisted and curved nanoscale shapes. Science *325*, 725–730. https://doi.org/10.1126/science.1174251.

Douglas, S.M., Dietz, H., Liedl, T., Hogberg, B., Graf, F., and Shih, W.M. (2009a). Self-assembly of DNA into nanoscale three-dimensional shapes. Nature *459*, 414–418. https://doi.org/10.1038/nature08016.

Douglas, S.M., Marblestone, A.H., Teerapittayanon, S., Vazquez, A., Church, G.M., and Shih, W.M. (2009b). Rapid prototyping of 3D DNA-origami shapes with caDNAno. Nucleic Acids Res. *37*, 5001–5006. https://doi.org/10.1093/nar/gkp436.

Franquelim, H.G., Khmelinskaia, A., Sobczak, J.P., Dietz, H., and Schwille, P. (2018). Membrane sculpting by curved DNA origami scaffolds. Nat. Commun. *9*, 811. https://doi.org/10.1038/s41467-018-03198-9.

Gerling, T., and Dietz, H. (2019). Reversible covalent stabilization of stacking contacts in DNA assemblies. Angew. Chem. Int. Ed. *58*, 2680–2684. https://doi.org/10.1002/anie.201812463.

Gerling, T., Wagenbauer, K.F., Neuner, A.M., and Dietz, H. (2015). Dynamic DNA devices and assemblies formed by shape-complementary, non-base pairing 3D components. Science *347*,

1446–1452. https://doi.org/10.1126/science.aaa5372.

Grome, M.W., Zhang, Z., Pincet, F., and Lin, C. (2018). Vesicle tubulation with self-assembling DNA nanosprings. Angew. Chem. Int. Ed. *57*, 5330–5334. https://doi.org/10.1002/anie.201800141.

Grossi, G., Dalgaard Ebbesen Jepsen, M., Kjems, J., and Andersen, E.S. (2017). Control of enzyme reactions by a reconfigurable DNA nanovault. Nat. Commun. *8*, 992. https://doi.org/10.1038/s41467-017-01072-8.

Hagiya, M., Konagaya, A., Kobayashi, S., Saito, H., and Murata, S. (2014). Molecular robots with sensors and intelligence. Acc. Chem. Res. *47*, 1681–1690. https://doi.org/10.1021/ar400318d.

Han, D., Pal, S., Nangreave, J., Deng, Z., Liu, Y., and Yan, H. (2011). DNA origami with complex curvatures in three-dimensional space. Science *332*, 342–346. https://doi.org/10.1126/science.1202998.

Hibino, K., Yoshikawa, Y., Murata, S., Saito, T., Zinchenko, A.A., and Yoshikawa, K. (2006). Na+ more strongly inhibits DNA compaction by spermidine (3+) than K+. Chem. Phys. Lett. *426*, 405–409. https://doi.org/10.1016/j.cplett.2006.05.120.

Jonchhe, S., Pandey, S., Emura, T., Hidaka, K., Hossain, M.A., Shrestha, P., Sugiyama, H., Endo, M., and Mao, H. (2018). Decreased water activity in nanoconfinement contributes to the folding of G-quadruplex and i-motif structures. Proc. Natl. Acad. Sci. U. S. A. *115*, 9539–9544. https://doi.org/10.1073/pnas.1805939115.

Kamiya, Y., and Asanuma, H. (2014). Light-driven DNA nanomachine with a photoresponsive molecular engine. Acc. Chem. Res. *47*, 1663–1672. https://doi.org/10.1021/ar400308f.

Kempter, S., Khmelinskaia, A., Strauss, M.T., Schwille, P., Jungmann, R., Liedl, T., and Bae, W. (2019). Single particle tracking and super-resolution imaging of membrane-assisted stop-and-go diffusion and lattice assembly of DNA origami. ACS Nano *13*. https://doi.org/10.1021/acsnano.8b04631-1002.

Khmelinskaia, A., Mucksch, J., Petrov, E.P., Franquelim, H.G., and Schwille, P. (2018). Control of membrane binding and diffusion of cholesteryl-modified DNA origami nanostructures by DNA spacers. Langmuir *34*, 14921–14931. https://doi.org/10.1021/acs.langmuir.8b01850.

Kielar, C., Ramakrishnan, S., Fricke, S., Grundmeier, G., and Keller, A. (2018). Dynamics of DNA origami lattice formation at solid-liquid interfaces. ACS Appl. Mater. Inter. *10*, 44844–44853. https://doi.org/10.1021/acsami.8b16047.

Kocabey, S., Kempter, S., List, J., Xing, Y., Bae, W., Schiffels, D., Shih, W.M., Simmel, F.C., and Liedl, T. (2015). Membrane-assisted growth of DNA origami nanostructure arrays. ACS Nano *9*, 3530–3539. https://doi.org/10.1021/acsnano.5b00161.

Krishnan, S., Ziegler, D., Arnaut, V., Martin, T.G., Kapsner, K., Henneberg, K., Bausch, A.R., Dietz, H., and Simmel, F.C. (2016). Molecular transport through large-diameter DNA nanopores. Nat. Commun. *7*, 12787. https://doi.org/10.1038/ncomms12787.

Kuchler, A., Yoshimoto, M., Luginbuhl, S., Mavelli, F., and Walde, P. (2016). Enzymatic reactions in confined environments. Nat. Nanotechnol. *11*, 409–420. https://doi.org/10.1038/nnano.2016.54.

Kurokawa, C., Fujiwara, K., Morita, M., Kawamata, I., Kawagishi, Y., Sakai, A., Murayama, Y., Nomura, S.i.M., Murata, S., Takinoue, M., and Yanagisawa, M. (2017). DNA cytoskeleton for stabilizing artificial cells. Proc. Natl. Acad. Sci. U S A. *114*, 7228–7233. https://doi.org/10.1073/pnas.1702208114.

Kuzuya, A., and Komiyama, M. (2009). Design and construction of a box-shaped 3D-DNA origami. Chem. Commun. *28*, 4182–4184. https://doi.org/10.1039/b907800b.

Langecker, M., Arnaut, V., Martin, T.G., List, J., Renner, S., Mayer, M., Dietz, H., and Simmel, F.C. (2012). Synthetic lipid membrane channels formed by designed DNA nanostructures. Science *338*, 932–936. https://doi.org/10.1126/science.1225624.

Lin, C., Perrault, S.D., Kwak, M., Graf, F., and Shih, W.M. (2013). Purification of DNA-origami nanostructures by rate-zonal centrifugation. Nucleic Acids Res. *41*, e40. https://doi.org/10.1093/nar/gks1070.

Liu, W., Zhong, H., Wang, R., and Seeman, N.C. (2011). Crystalline two-dimensional DNA-origami arrays. Angew. Chem. Int. Ed. *50*, 264–267. https://doi.org/10.1002/anie.201005911.

Mingeot-Leclercq, M.P., Deleu, M., Brasseur, R., and Dufrene, Y.F. (2008). Atomic force microscopy of supported lipid bilayers. Nat. Protoc. *3*, 1654–1659. https://doi.org/10.1038/nprot.2008.149.

Praetorius, F., Kick, B., Behler, K.L., Honemann, M.N., Weuster-Botz, D., and Dietz, H. (2017). Biotechnological mass production of DNA origami. Nature *552*, 84–87. https://doi.org/10.1038/nature24650.

Rajendran, A., Endo, M., Katsuda, Y., Hidaka, K., and Sugiyama, H. (2011). Programmed two-dimensional self-assembly of multiple DNA origami jigsaw pieces. ACS Nano *5*, 665–671. https://doi.org/10.1021/nn1031627.

Ramakrishnan, S., Subramaniam, S., Stewart, A.F., Grundmeier, G., and Keller, A. (2016). Regular nanoscale protein patterns via directed adsorption through self-assembled DNA origami masks. ACS Appl. Mater. Inter. *8*, 31239–31247. https://doi.org/10.1021/acsami.6b10535.

Rothemund, P.W.K. (2006). Folding DNA to create nanoscale shapes and patterns. Nature *440*, 297–302. https://doi.org/10.1038/nature04586.

Sakamoto, S., Komatsu, T., Watanabe, R., Zhang, Y., Inoue, T., Kawaguchi, M., Nakagawa, H., Ueno, T., Okusaka, T., Honda, K., et al. (2020). Multiplexed single-molecule enzyme activity analysis for counting disease-related proteins in biological samples. Sci. Adv. *6*, eaay0888. https://doi.org/10.1126/sciadv.aay0888.

Schneider, C.A., Rasband, W.S., and Eliceiri, K.W. (2012). NIH Image to ImageJ: 25 years of image analysis. Nat. Methods *9*, 671–675. https://doi.org/10.1038/nmeth.2089.

Shrestha, P., Jonchhe, S., Emura, T., Hidaka, K., Endo, M., Sugiyama, H., and Mao, H. (2017). Confined space facilitates G-quadruplex formation. Nat. Nanotechnol. *12*, 582–588. https://doi.org/10.1038/nnano.2017.29.

Suzuki, Y., Endo, M., and Sugiyama, H. (2015). Lipid-bilayer-assisted two-dimensional self-assembly of DNA origami nanostructures. Nat. Commun. *6*, 8052. https://doi.org/10.1038/ncomms9052.

Suzuki, Y., Sakai, N., Yoshida, A., Uekusa, Y., Yagi, A., Imaoka, Y., Ito, S., Karaki, K., and Takeyasu, K. (2013). High-speed atomic force microscopy combined with inverted optical microscopy for studying cellular events. Sci. Rep. *3*, 2131. https://doi.org/10.1038/srep02131.

Thomsen, R.P., Malle, M.G., Okholm, A.H., Krishnan, S., Bohr, S.S.R., Sorensen, R.S., Ries, O., Vogel, S., Simmel, F.C., Hatzakis, N.S., and Kjems, J. (2019). A large size-selective DNA nanopore with sensing applications. Nat. Commun. *10*, 5655. https://doi.org/10.1038/s41467-019-13284-1.

Tikhomirov, G., Petersen, P., and Qian, L. (2017). Fractal assembly of micrometre-scale DNA origami arrays with arbitrary patterns. Nature *552*, 67–71. https://doi.org/10.1038/nature24655.

Uchihashi, T., Kodera, N., and Ando, T. (2012). Guide to video recording of structure dynamics and dynamic processes of proteins by high-speed atomic force microscopy. Nat. Protoc. *7*, 1193–1206. https://doi.org/10.1038/nprot.2012.047.

Wagenbauer, K.F., Sigl, C., and Dietz, H. (2017). Gigadalton-scale shape-programmable DNA assemblies. Nature *552*, 78–83. https://doi.org/10.1038/nature24651.

Willner, E.M., Kamada, Y., Suzuki, Y., Emura, T., Hidaka, K., Dietz, H., Sugiyama, H., and Endo, M. (2017). Single-molecule observation of the photoregulated conformational dynamics of DNA origami nanoscissors. Angew. Chem. Int. Ed. *56*, 15324–15328. https://doi.org/10.1002/anie.201708722.

Woo, S., and Rothemund, P.W.K. (2011). Programmable molecular recognition based on the geometry of DNA nanostructures. Nat. Chem. *3*, 620–627. https://doi.org/10.1038/nchem.1070.

Woo, S., and Rothemund, P.W.K. (2014). Self-assembly of two-dimensional DNA origami lattices using cation-controlled surface diffusion. Nat. Commun. *5*, 4889. https://doi.org/10.1038/ncomms5889.

Xin, Y., Shen, B., Kostiainen, M.A., Grundmeier, G., Castro, M., Linko, V., and Keller, A. (2021). Scaling up DNA origami lattice assembly. Chem. Eur. J. *27*, 8564–8571. https://doi.org/10.1002/chem.202100784.

Yoshida, A., Sakai, N., Uekusa, Y., Imaoka, Y., Itagaki, Y., Suzuki, Y., and Yoshimura, S.H. (2018). Morphological changes of plasma membrane and protein assembly during clathrin-mediated

endocytosis. PLoS Biol. *16*, e2004786. https://doi.org/10.1371/journal.pbio.2004786.

Yoshimura, Y., and Fujimoto, K. (2008). Ultrafast reversible photo-cross-linking reaction: toward in situ DNA manipulation. Org. Lett. *10*, 3227–3230. https://doi.org/10.1021/ol801112j.

Zhang, T., Hartl, C., Frank, K., Heuer-Jungemann, A., Fischer, S., Nickels, P.C., Nickel, B., and Liedl, T. (2018). 3D DNA origami crystals. Adv. Mat. *30*, e1800273. https://doi.org/10.1002/adma.201800273.

Zhao, Z., Fu, J., Dhakal, S., Johnson-Buck, A., Liu, M., Zhang, T., Woodbury, N.W., Liu, Y., Walter, N.G., and Yan, H. (2016). Nanocaged enzymes with enhanced catalytic activity and increased stability against protease digestion. Nat. Commun. *7*, 10619. https://doi.org/10.1038/ncomms10619.

Zhao, Z., Liu, Y., and Yan, H. (2011). Organizing DNA origami tiles into larger structures using preformed scaffold frames. Nano Lett. *11*, 2997–3002. https://doi.org/10.1021/nl201603a.

STAR★METHODS

KEY RESOURCES TABLE

REAGENT or RESOURCE	SOURCE	IDENTIFIER
Chemicals, peptides, and recombinant proteins		
Magnesium chloride	NIPPON GENE, Japan	310–90361
Tris-HCl (pH 8.0)	NIPPON GENE, Japan	312–90061
5×TBE	NIPPON GENE, Japan	318–90041
Ethylendiaminetetraacetic acid (EDTA), pH 8.0	Thermo Fisher Scientific, USA	15575–038
SYBR™ Gold Nucleic Acid Gel Stain	Thermo Fisher Scientific, USA	S11494
Glycerol	Wako, Japan	072–00626
Agarose S	Wako, Japan	312–01193
Streptavidin	Wako, Japan	198–17861
1,2-Dioleoyl-*sn*-glycero-3-phosphocholine (DOPC)	Avanti Polar Lipids, USA	850375C-25mg
Oligonucleotides		
Unmodifed ssDNA strands, see Tables S1–S3	Eurofins Japan, Japan	https://www.eurofins.co.jp
Biotin-labeled DNA strands, see Table S4	Eurofins Japan, Japan	https://www.eurofins.co.jp
Software and algorithms		
caDNAno2	Douglas et al. 2009b	https://cadnano.org
ImageJ	Schneider et al. 2012	https://imagej.nih.gov/ij/
Other		
Scaffold ssDNA (p8064)	tilibit nanosystems, Germany	https://www.tilibit.com
100 kDa Amicon Ultra filters	Merck, Germany	UFC510096
himac 2.2PA TUBE	Koki Holdings, Japan	S300536A
Micro ultracentrifuge	Hitachi, Japan	himac CS150GXII
Swing rotor	Hitachi, Japan	S55S-2017
Gel imager	BIO-RAD	ChemiDoc™ MP Imaging System (170–8280)
Mica	Furuuchi chemical, Japan	Clear mica, φ3.0 mm
High-speed atomic force microscopy	Olympus, Japan	BIXAM
Cantilever	Nanoworld, Switzerland	USC-F0.8-k0.1-T12

RESOURCE AVAILABILITY

Lead contact

Further information and requests for resources should be directed to and will be fulfilled by the corresponding author: Yuki Suzuki (yuki.suzuki.e6@tohoku.ac.jp).

Materials availability

This study did not generate any new reagents.

Data and code availability

- Data reported in this paper will be shared by the lead contact upon request.
- This study does not report any original code.
- Any additional information required to reanalyze the data reported in this paper is available from the lead contact upon request.

METHOD DETAILS

Preparation of DNA origami structures

The 8064 nt scaffold single-stranded DNA (p8064) was purchased from tilibit Nanosystems (Garching, Germany). All staple strands were purchased from Eurofins Genomics (Tokyo, Japan). DNA origami structures were designed using caDNAno2 software (Douglas et al., 2009b) (Figure S1). DNA origami structures were folded by mixing 10 nM scaffold ssDNA (p8064) with ~40 nM staple strands in 20 μL of folding buffer containing 5 mM Tris-HCl (pH 8.0), 15 mM $MgCl_2$, and 1 mM EDTA. The mixture was incubated at 65°C for 15 min, then annealed by reducing the temperature from 60°C to 45 °C at a rate of 1.0°C/h.

Purification of DNA origami by density gradient centrifugation

DNA origami structures were purified using a glycerol gradient (Lin et al., 2013). To prepare a linear glycerol gradient (5–45%, v/v), nine layers (200 μL per layer) of glycerol solution in 1 × TE-Mg buffer (5 mM Tris-HCl [pH 8.0], 15 mM $MgCl_2$, and 1 mM EDTA) were carefully added into a 2.2 mL ultracentrifuge tube with 5% concentration decrement per layer, starting with a 45% glycerol solution at the bottom. The tube was incubated overnight at 25°C to prepare a glycerol gradient. A solution of DNA origami nanostructures (200 μL) containing 5% glycerol was then loaded on top of the glycerol gradient. The tube was then centrifuged at 50,000 rpm (214,288 ×g) for 1 h at 4°C using an ultracentrifuge (himac CS150GXII, Hitachi, Tokyo, Japan) equipped with a swing-rotor (S55S-2017, Hitachi, Tokyo, Japan). After centrifugation, 15 fractions (133 μL each) were collected sequentially from the top to bottom of the tube. Aliquots of each fraction were subjected to agarose gel electrophoresis (Figure S2). The fractions exhibiting the target bands were mixed and concentrated using Amicon Ultra-0.5 mL centrifugal filters (MWCO 100 kDa) (Merck KGaA, Darmstadt, Germany). The glycerol-containing buffer was also replaced with glycerol-free buffer during ultracentrifugation.

Agarose gel electrophoresis

The samples were loaded for electrophoresis on a 1.0% or 1.5% agarose gel containing 5 mM $MgCl_2$ in a 0.5× TBE (Tris-borate-EDTA) buffer solution (pH 8.0) at 50 V and 4°C. The gels were then imaged with ChemiDOC MP (Bio-Rad Laboratories, Inc., CA, USA) using SYBR Gold nucleic acid gel stain (Thermo Fisher Scientific, MA, USA) as the staining dye.

Preparation of mica-supported lipid bilayers

Mica-supported lipid bilayers (mica-SLBs) were prepared by employing a vesicle fusion method (Mingeot-Leclercq et al., 2008), as previously described (Suzuki et al., 2015; Uchihashi et al., 2012), with some modifications. Lipid dry films were prepared by adding 20 μL of 10 mg/mL 1,2-Dioleoyl-sn-glycero-3-phosphocholine (DOPC) (Avanti Polar Lipids, AL, USA) solution dissolved in chloroform in a round-glass tube, followed by overnight drying under vacuum with argon gas. Ultrapure water (400 μL) was then added to the dried lipid film to obtain a lipid concentration of 0.5 mg/mL. The glass tubes were vortexed and sonicated to generate small unilamellar vesicles (SUVs). Mica-SLBs were formed by depositing 2 μL of the SUV solution, followed by the addition of 1 μL of buffer containing 20 mM Tris-HCl (pH 7.6), 10 mM $MgCl_2$, and 1 mM EDTA onto freshly cleaved mica disks, with a diameter of 3.0 mm (Furuuchi Chemical, Tokyo, Japan). To prevent drying of the bilayers, the samples were incubated at room temperature (25°C) in a sealed container containing a piece of Kimwipe moistened with Milli-Q water. After 30 min of adsorption on mica, the sample was rinsed with buffer to remove the unadsorbed SUVs. The procedure, from deposition to rinsing, was repeated twice to completely coat the mica surface with a bilayer.

Lipid bilayer-surface-assisted self-assembly of hexagonal 3D origami structures

A drop (3 μL) of hexagonal 3D DNA origami (3D-Hx) nanostructures in folding buffer (10 nM) was deposited onto the preformed SLB. After 5 min of incubation in the sealed container described above, the sample was soaked in 120 μL of buffer containing 20 mM Tris-HCl (pH 7.5), 1 mM EDTA, and 15 mM $MgCl_2$ without surface rinsing, and then further incubated for 30 min at room temperature. Surface-assisted self-assembly was then induced by adding an appropriate volume of 1 M $MgCl_2$ to the buffer, to a final concentration of 50 mM. After an additional 60 min of incubation, the sample was subjected to atomic force microscopy (AFM) imaging in the same buffer. For time-lapse imaging of the dynamic events during self-assembly, this additional incubation was omitted, and imaging was started immediately after the addition of $MgCl_2$.

AFM observation

High-speed AFM (HS-AFM) imaging was performed using tip scan high-speed AFM (BIXAM, Olympus, Tokyo, Japan), which was improved based on a previously developed prototype AFM (Suzuki et al., 2013; Yoshida et al., 2018). Small cantilevers (9 μm long, 2 μm wide, and 100 nm thick) with a spring constant of 0.1 N/m (USC-F0.8-k0.1-T12; Nanoworld, Neuchâtel, Switzerland) were applied. The images were collected at a scan rate of 0.5 frames per second (fps). The image sequences were analyzed using AFM scanning software (Olympus) and ImageJ software (http://ImageJ.nih.gov/ij/) (Schneider et al., 2012).